Optimization of process parameters in laser beam powder bed fusion using surface texture and density of Inconel 718

Yusuke TACHIBANA*, Toshi-Taka IKESHOJI**, Makiko YONEHARA** and Hideki KYOGOKU**

*Graduate School of Systems Engineering, Kindai University
1 Takaya-Umenobe, Higashihiroshima, Hiroshima 739-2116, Japan
**Fundamental Technology for Next Generation Research Institute, Kindai University
& Kindai University Hiroshima Branch, Technology Research Association for Future Additive Manufacturing
1 Takaya-Umenobe, Higashihiroshima, Hiroshima 739-2116, Japan
E-mail: kyogoku@hiro.kindai.ac.jp

Abstract

This study aims to optimize the process parameters for PBF-LB of Inconel 718 using the surface texture and density of the as-built specimen to fabricate high-quality products. In order to achieve this aim, the melting and solidification phenomena of the melt pool were examined using a high-speed camera, and the process map of laser power and scan speed was constructed by evaluating the surface texture and density of the as-built specimen to optimize the process parameters. In addition, the mechanical properties of the as-built specimens fabricated at the optimum process parameter derived from the process map were examined. Consequently, it was found that the optimum process parameter should be determined by consideration of the melting and solidification phenomena because the phenomena such as spattering and instability of the melt pool change with the process parameters. It was also found that the morphology of the track is affected by the spot size of the laser beam. It was revealed that the similarity of the process maps evaluated by surface texture and density of the specimens results in the correlation between the surface texture and the density. The optimum laser power and scan speed can be determined using the process maps evaluated by the surface texture and density of the specimens. The as-built specimen fabricated at the optimum process parameter showed anisotropic tensile behavior, and the tensile strength of the transverse specimen was higher than that of the longitudinal specimen. The tensile properties of the as-built specimen fabricated in this work were similar to those of the as-built specimen reported by the other works.

Keywords : Additive manufacturing, Laser beam powder bed fusion, Ni-based superalloy, High-speed imaging, Process map, Tensile properties

1. Introduction

Recently, additive manufacturing (AM) technology has much attention in the aerospace, medical, and power generation industries. Especially, laser beam powder bed fusion (PBF-LB) known as selective laser melting (SLM), which is one of the AM technology, has been widely applied because PBF-LB allows for the manufacturing of three-dimensional complex-shaped metallic products, which are impossible to manufacture using a conventional process, through CAD data easily. In addition, PBF-LB has been applied to a great variety of alloys such as stainless steel, titanium alloy, aluminum alloy, nickel-based superalloy. In particular, nickel-based superalloy is used for a wide variety of applications in the field of aerospace, chemical, and power generation industries because of its superior corrosion resistance and heat resistance (Gibson, et al., 2010).

A Ni-based superalloy is an alloy strengthened the matrix of the γ phase (fcc) by precipitates. Inconel 718 (IN 718), which is one of the most useful superalloys, is Ni-Cr-Fe alloy having high-temperature strength with corrosion resistance, superior fatigue strength and creep strength, and superior weldability (Fu et al., 2009, ASM Handbook, 1998). Therefore, this alloy applies to gas turbine blades, aircraft engine parts, and nuclear engineering parts.

There are lots of reports on PBF-LB process of IN 718 (Amato et al., 2012, Chlebus et al., 2015, Zhang et al., 2015, Aydinoez et al., 2016, Ferber et al., 2018, Sames et al., 2017, Kirka et al., 2017, Jia et al, 2014, 4 Ni et al., 2017, Nadammal et al., 2017). Amato et al. (2012) investigated the microstructure of IN 718 fabricated by PBF-LB process and the effect of heat treatment on the microstructure and tensile properties of the alloy. As a result, they reported that the tensile properties of the as-built and heat-treated alloys are almost equal to those of the wrought alloy. Chlebus et al. (2015) investigated the microstructures of the as-built and heat-treated IN 718 and the effect of microstructure on the mechanical properties of the alloy. It was reported that the microstructure of the as-built IN 718 fabricated by PBF-LB process consists of columnar grains of γ (fcc) matrix in the build direction and arrays of γ'' (bct or $D0_{22}$) Ni_3Nb precipitates (Amato et al., 2012, Chlebus et al., 2015, Zhang et al., 2015, Aydinoez et al., 2016, Ferber et al., 2018, Sames et al., 2017, Kirka et al., 2017) investigated the effect of heat treatment on the microstructure by means of TEM and concluded that the heat treatment strengthens the matrix by precipitates of Laves phase and carbides. Farber et al. (2018) reported on the correlation of mechanical properties to the microstructure of IN 718 performed heat treatment including hot isostatic pressing (HIP). Moreover, Sames et al. (2017) and Kirka et al. (2017) reported on the microstructure and mechanical properties of IN 718 fabricated by PBF-LB and electron beam powder bed fusion (PBF-EB), and the microstructure of the as-built IN 718 fabricated by PBF-LB is substantially different from that of the as-built IN 718 fabricated by PBF-EB due to the difference in cooling rate.

Jia et al. (2014) and Ni et al. (2017) investigated the effect of energy density on the density, microstructure, and tensile properties of the as-built IN 718. Nadammal et al. (2017) investigated the effect of hatching pitch on the development of microstructure, texture, and residual stresses of the as-built specimen, as well. They described that the variation in temperature gradient with hatching pitch influenced the microstructure, texture, and residual stress. Carter et al. (2015) reported on the optimization of process parameters of PBF-LB for CMSX486 Ni-based superalloy using the analysis of variance (ANOVA) to produce a void-free alloy and to reduce the cracking density. They described that a validation sample showed a good agreement to the predicted for void percent using the predicted optimum condition. Thus, the influence of the process parameters on the generation of internal defects or the density of the parts has been frequently reported (Kyogoku and Ikeshoji, 2020).

The process map of the laser power and scan speed are frequently used to determine the optimum process parameter (Yakout et al., 2017). However, there are few reports on the effect of process parameters on the density and surface roughness of the IN 718 fabricated by PBF-LB process using the process map. Recently, machine learning or deep learning have been applied to optimize the process parameters (Baturynska et al., 2018, Gobert et al., 2018, Aoyagi et al., 2019, Caggiano et al., 2019) and to predict the quality of parts (Hertlein et al., 2020). Gobert et al. (2018) also applied a supervised machine learning to detect defects during powder bed fusion process. Aoyagi et al. (2019) applied a support vector machine to construct a process map on the PBF-EB process.

This study aims to optimize the process parameters for PBF-LB of IN 718 by the surface roughness and density of the as-built specimen to fabricate high quality products. In order to achieve this aim, the melting and solidification phenomena of the melt pool were investigated using a high-speed camera, and the process map between laser power and scan speed was constructed by evaluating the surface texture and density of the as-built specimen to optimize the process parameters. In addition, the mechanical properties of the as-built parts fabricated at the optimum process parameter derived from the process map were examined.

2. Experimental procedures

2.1 PBF-LB proto-type machine

A PBF-LB proto-type machine equipped with a 1 kW single-mode fiber laser (wave length:1.07 µm) was employed for fabrication of the specimens. The laser spot diameter was set to $d_{90} = ø100$ µm ($d_{86.5} = ø93$ µm). In addition, Photoron FASTCAM SA-Z high-speed camera, and FLIR thermo-viewer were employed for monitoring the melting and solidification phenomena. The high-speed camera can record a 1×5 mm area at a frame rate of 50,000 fps.

2.2 Powder and specimen

A gas-atomized IN 718 powder was prepared in this study. The mean particle diameter of IN718 powder was around 30 µm. The SEM image and chemical composition of this powder are shown in Fig. 1 and Table 1, respectively.

In order to construct the process map of laser power and scan speed, (a) single track of 10 mm in length and (b) cuboid specimens of $16.0 \times 12.2 \times 15.0$ mm were fabricated as shown in Fig. 2.

2.3 Experimental method

The surface texture of the as-built cuboid specimen was observed using JEOL JSM-7800F scanning electron microscopy (SEM) and the ISO 25178-2 areal surface texture parameters were measured using the coherence scanning interferometry (CSI) system (Zygo NewView 9000). The surface texture was evaluated using the arithmetical mean height S_a and the root mean square height S_q defined by ISO 25178-2 (2021) as shown in Eq. (1) and (2), respectively.

$$S_a = \frac{1}{A} \iint |Z(x,y)| \, dxdy \tag{1}$$

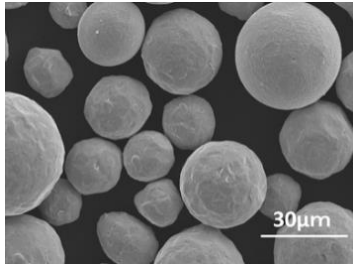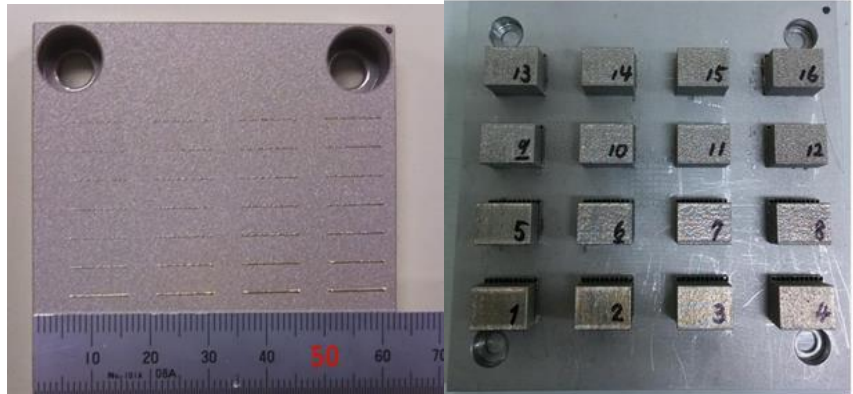$$S_q = \sqrt{\frac{1}{A} \iint z^2(x,y)dxdy} \tag{2}$$

Fig.1 The SEM image of IN 718 powder

(a) Single track   (b) Cuboid specimen

Fig. 2 The as-built specimens of IN 718

Table 1 Chemical composition of IN 718 powder

Element	C	Si	Mn	P	S
(mass %)	0.004	0.160	0.170	0.003	0.002
Element	Al	Ti	Nb	Co	B
(mass %)	0.470	0.088	5.160	<0.010	<0.001

The melting and solidification phenomena of the melt pool were observed using Photoron FASTCAM SA-Z high-speed camera.

The density of the as-built specimens was measured by the Archimedes method. The relative density was calculated using the reference value of 8.19 g/cm^3. The microstructure was observed using an optical microscope (OM) after electrolytic etching in 10% oxalic acid solution. The as-built tensile test specimens fabricated at the optimum condition. The tensile test was performed using an Instron tensile testing machine.

3. Results and discussions
3.1 Process map evaluated by surface roughness of single tracks
3.1.1 Fabrication conditions

It is significant to investigate the optimum process parameters to fabricate high-quality products. Notably, the main process parameters are the laser power P, the scan speed v, the hatching pitch h, and the layer thickness t; besides the power density E_L and the volumetric energy density E_V are used well as the index summarizing these process parameters.

First of all, the coverage of laser power and scan speed was narrowed down by the fabrication of single tracks to optimize these parameters. In the case of single tracks, the power density E_L (J/mm^2) defined as Eq. (3) was applied.

$$E_L = P / vd, \tag{3}$$

where d is the spot size of the laser beam.

The fabrication conditions of single tracks are summarized in Table 2.

Table 2 Fabrication conditions

	Condition A	Condition B	Condition C
Laser power (W)	100 - 400	100 - 400	100 - 400
Scan speed (mm/s)	100 - 1400	100 - 1400	100 - 1400
Layer thickness (mm)	0.05	0.05	0.05
Spot diameter (mm)	0.10	0.20	0.30
Power density (J/mm^2)	0.7 - 40	0.4 - 20	0.2 - 13.3

3.1.2 The melting and solidification phenomena during laser radiation

The melting and solidification phenomena during laser radiation were observed using a high-speed camera by changing the laser power and the scan speed. The representative melting and solidification phenomena at a laser power of 300 W and a scan speed between 300 mm/s and 1400 mm/s are shown in Fig. 3. In the case of 300 mm/s in Fig. 3(a), the melt pool is so wide and swells greatly, and a lot of spatters spread out owing to a higher energy density. In the case of 500 mm/s in Fig. 3(b), however, the melt pool is so stable and slightly swells, and a few spatters spread out due to a suitable energy density. On the other hand, in the case of 1400 mm/s in Fig. 3(c), the melt pool is unstable, and a balling effect takes place by Rayleigh instability owing to lower energy density (Kyogoku and Ikeshoji, 2020).

(a) Laser power: 300 W, Scan speed: 300 mm/s

(b) Laser power: 300 W, Scan speed: 500 mm/s

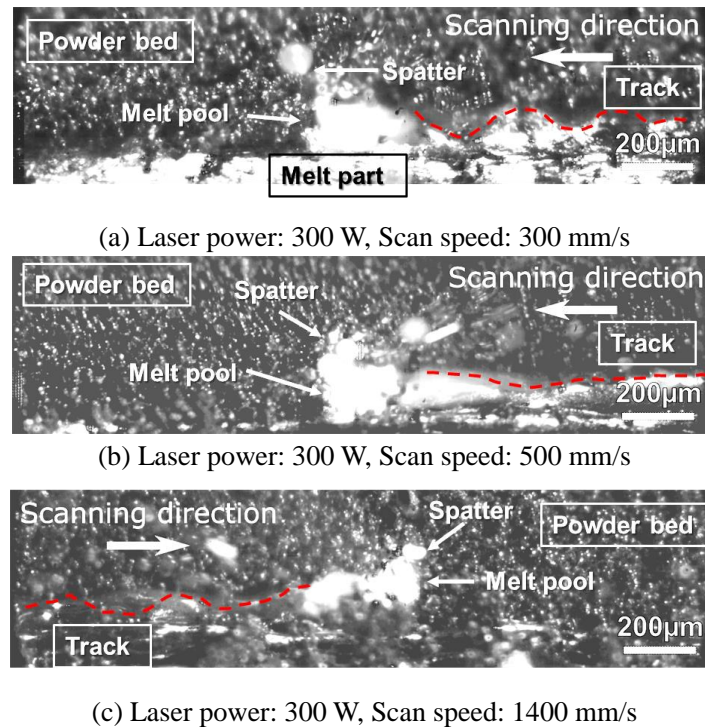(c) Laser power: 300 W, Scan speed: 1400 mm/s
Fig.3 The representative melting and solidification phenomena during laser radiation

Grasso and Colosimo (2017) reviewed on the process defects and in-situ monitoring methods in PBF-LB. The melting and solidification phenomena during laser radiation have been investigated by experiments as well as using numerical simulation. King et al. (2014, 2015), Khairallah et al. (2016, 2020), Matthews et al. (2016), and Ly et al. (2017) revealed the mechanisms of generation of defects during laser radiation not only by the observation using a high-speed camera and a thermo-viewer but also by the numerical simulation. Ikeshoji et al. (2018) investigate the melting and solidification phenomena of pure coper using a high-speed camera and numerical simulation. Furumoto et al. (2018) investigated the melt pool behavior by high-speed camera in PBF-LB process. Kyogoku and Ikeshoji (2020) investigated the melting and solidification phenomena using a high-speed camera and a thermo-viewer and reported a similar melting and solidification phenomena that occurred during laser radiation. Moreover, Zhao et al. (2017) and Cunningham (2019) conducted the real-time in-situ monitoring of the PBF-LB process by employing the high-speed synchrotron hard X-ray imaging technique. They exhibited the results of the dynamic X-ray images of the PBF-LB

process in the cases of conduction mode melting and keyhole mode melting. Martin et al. (2019) and Forein et al. (2020) investigated the dynamics of the formation of keyhole pores using X-ray imaging technique. Consequently, instability of melt pool and spatters derived from unsuitable process parameters bring about internal defects such as a lack of fusion and pores.

Accordingly, it is significant to determine the optimum process parameter by consideration of the melting and solidification phenomena because the phenomena such as spattering and instability of the melt pool drastically changes with the process parameters.

3.1.3 Influence of the spot size of laser beam

The influence of spot size of laser beam, which is one of the most important process parameters, on the single-track morphology was investigated. The SEM images of single tracks scanned by changing at a laser power of 100 W - 400 W and a scan speed of 100 mm/s - 1400 mm/ s and the process map of laser power and scan speed evaluated by the morphology of single track are exhibited at various spot sizes of 0.1 mm, 0.2 mm and 0.3 mm in Fig.4. In this figure, a continuous and stable track and a continuous and unstable track are indicated by the symbols of ● and ▲, respectively. The morphology of tracks becomes thinner and unstable with a decrease in laser power and an increase in scan speed, namely a decrease in power density at any spot size. In the case of 0.3 mm, the region in which a continuous and stable track can be obtained becomes narrower. This may be caused by the lowering of the power density calculated by Eq. (1) due to broadening the area of laser radiation. It is well known that the spot size of the laser beam affects the morphology of the melt pool. McLouth et al. (2018) reported on the influence of spot size, that is, the power density by changing the focal shift on the morphology of the melt pool while keeping the laser parameters constant. As a result, because the morphology of melt pool changes, the microstructure of IN 718 parts is characterized. Also, Bean et al. (2018) reported on the effect of change of energy density by laser focus shift on the surface roughness, density, and porosity of IN 718 parts.

Thus, it was found that the morphology of the tracks is affected by the spot size of laser beam, and the process window of spot size of 0.1 mm and 0.2 mm is wider than that of 0.3 mm. Therefore, the spot size of 0.2 mm was selected in this study.

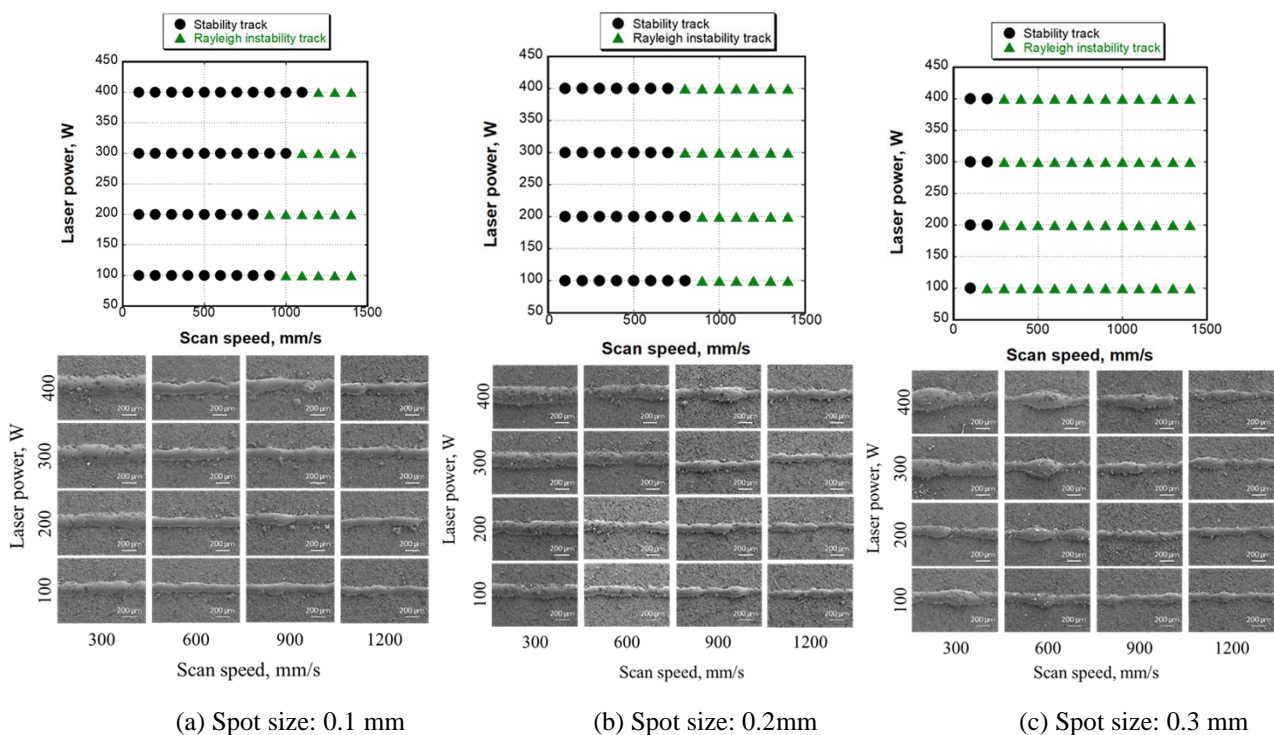(a) Spot size: 0.1 mm   (b) Spot size: 0.2mm   (c) Spot size: 0.3 mm

Fig.4 The SEM images of single tracks scanned at various spot sizes and the process map of laser power and scan speed evaluated by the morphology of single tracks

3.1.4 3D-Process map evaluated by the surface roughness of single tracks

The 3D-Process map of laser power and scan speed evaluated by the surface roughness of single tracks obtained at a spot size of 0.2 mm is depicted in Fig. 5. The arithmetical mean roughness R_a of single tracks fabricated by changing the laser power and scan speed is shown in Fig. 5(a). R_a means the height of single track because R_a was measured the surface of a build plate as a datum level. The height of single tracks increases with increasing power density. As shown in Fig. 5(b), R_a increases with increasing the laser power and decreasing the scan speed, and the maximum of R_a is approximately 100 µm. This result suggests that the recoating blade collides with a track fabricated in the red region of higher laser power and slower scan speed of the process map because, if the set layer thickness t is 50 µm and the apparent density is 60%, the actual powder layer thickness is approximately 70 µm.

Thus, it was found that the height of a single track is greatly affected by laser power and scan speed, that is, power density.
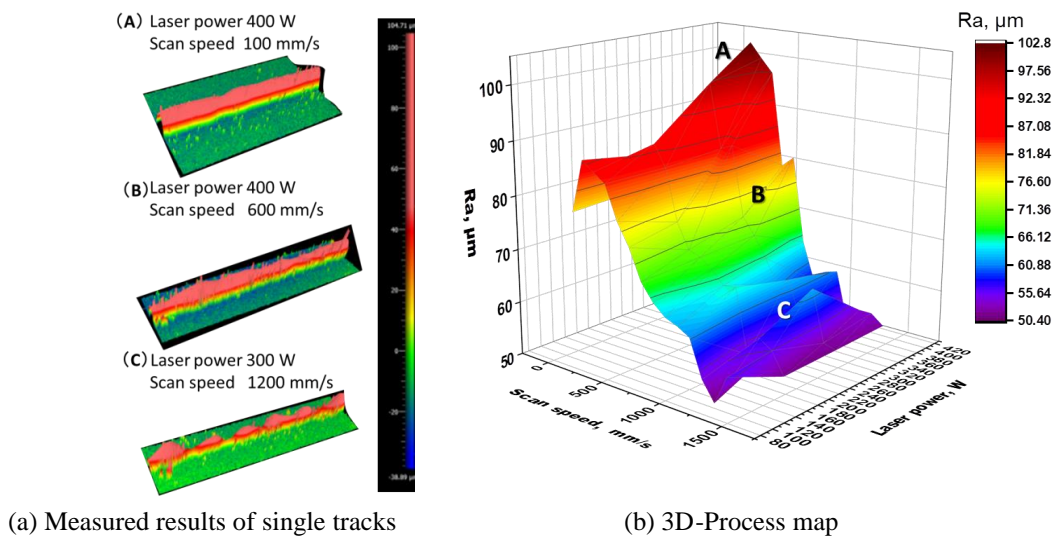

(a) Measured results of single tracks   (b) 3D-Process map

Fig.5 The 3D-Process map of laser power and scan speed evaluated by the morphology of single tracks

3.2 Process map of laser power and scan speed evaluated by surface texture and density

The process parameters of the laser power and the scan speed were investigated by observation of surface texture of the as-built cuboid specimens because the region of laser power and scan speed, in which can be fabricated a stable track, was found out from Fig. 4. The fabrication conditions are summarized in Table 3. The volumetric energy density E_v was calculated by the following equation;

$$E_v=P/vht, \tag{4}$$

where P is the laser power [W], v is the scan speed [mm/s], h is the hatching pitch [mm], and t is the layer thickness [mm].

Table 3 Fabrication conditions

Laser power (W)	250, 300, 350, 400
Scan speed (mm/s)	500, 600, 700, 800
Hatching pitch (mm)	0.15
Layer thickness (mm)	0.05
Spot diameter (mm)	0.20
Energy density (J/mm^3)	41.7 – 106.7

The variation of the arithmetical mean height S_a of the as-built cuboid specimens as a function of the volumetric energy density E_v is depicted in Fig. 6. In the case of an energy density of less than 50 J/mm^3, S_a is about 25 µm and the surface shows intense uneven-even formed by balling effect and spattering because of a lack of energy density as

shown in Fig. 6(A). On the other hand, in the case of more than 90 J/mm^3, S_a is about 20 µm, and the surface shows remarkably uneven accompanying with large spatters because of excess energy density as shown in Fig. 6(D). These results correspond to the behavior of the melt pool, such as instability melt pool and spattering as mentioned above. It was revealed that the suitable energy density is around 80 J/mm^3 to fabricate the specimens having a smooth surface. In the case of laser power of 300 W and a scan speed of 500 mm/s (a volumetric energy density of 80 J/mm^3), the minimum S_a is approximately 10 µm.

Thus, the as-built cuboid specimen having a smooth surface could be fabricated at a laser power of 300 W and a scan speed of 500 mm/s (an energy density of 80 J/mm^3).
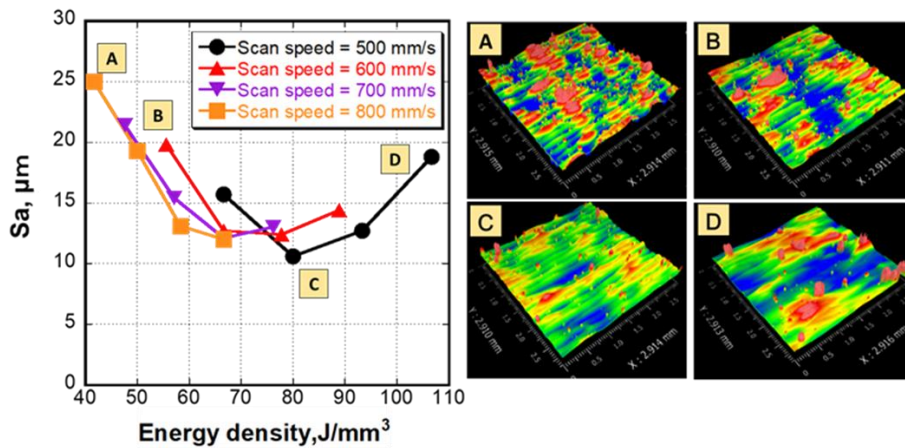

Fig.6 The variation of the surface texture of cuboid specimens as a function of the volumetric energy density

Additionally, the variation of the relative density as a function of the volumetric energy density is exhibited in Fig. 7. The relative density increases with increasing energy density, and the maximum relative density is 99.94% at 80 J/mm^3. The 3D-Process map of laser power and scan speed evaluated by relative density is depicted in Fig. 8. The relative density reaches the maximum at a laser power of 350 W and a scan speed of 500 mm/s, respectively. The microstructures of the as-built specimens indicated by the symbols of A and B in Fig. 8 are also presented. In the case of the specimen A, few pores are observed, while in the case of the specimen B, lack of fusion defects are visible. The lack of fusion defects could be caused by unstable track due to lower energy density as shown in Fig. 5 and Fig.7.

As a result, the as-built cuboid specimen having the maximum density of 99.94% was able to be fabricated at a laser power of 300 W and a scan speed of 500 mm/s (an energy density of 80 J/mm^3).
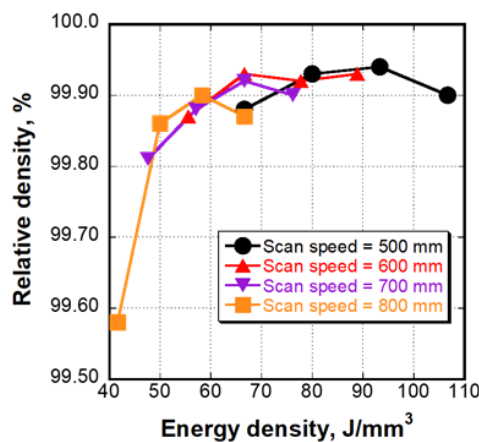

Fig.7 The variation of the relative density as a function of the volumetric energy density

The CSI images and surface texture of the specimens fabricated at various laser power and scan speed are presented in Fig. 9. The numerical values of the upper left, the lower left and the lower right in the CSI images indicate

E_v, S_a and S_q, respectively. In addition, the schematic process map of laser power and scan speed including the representative SEM images and the CSI images are depicted in Fig. 10. As described in section 3.1.2, the A region in the process map is the high laser power and low scan speed, that is, the high energy density area. A high laser power leads to a keyhole phenomenon and the high energy density results in generation of internal defects and spatters due to the heavy swelling of melt pool. Therefore, as shown in Fig. 10, lots of spatters are on the surface of the specimen, and the surface greatly swells in the whole area and shows remarkable unevenness as S_a is 18.8 µm and S_q is 180.2 µm. The center area of the B region corresponds to the suitable fabrication condition region (process window), in which the melt pool is stable, that is, the conduction mode in welding. The SEM image shows that the surface texture with few spatters form by almost uniform tracks and the CSI image shows evenness of the surface as S_a is 10.6 µm and S_q is 153.0 µm. In the C region, lack of fusion defects generate owing to insufficient energy density. The SEM image shows ununiform tracks and the CSI image presents the severe unevenness of the surface as S_a is 25.0 µm and S_q is 141.3 µm. In the D region, lack of fusion defects tend to generate because the melt pool is unstable and the balling effect occurs due to higher laser power and higher scan speed. The SEM image shows wider and ununiform tracks and the CSI image exhibits the undulated and remarkable uneven surface as S_a is 12.0 µm and S_q is 169.8 µm.

(a) 3D-Process map   (b) Microstructures of the as-built specimen
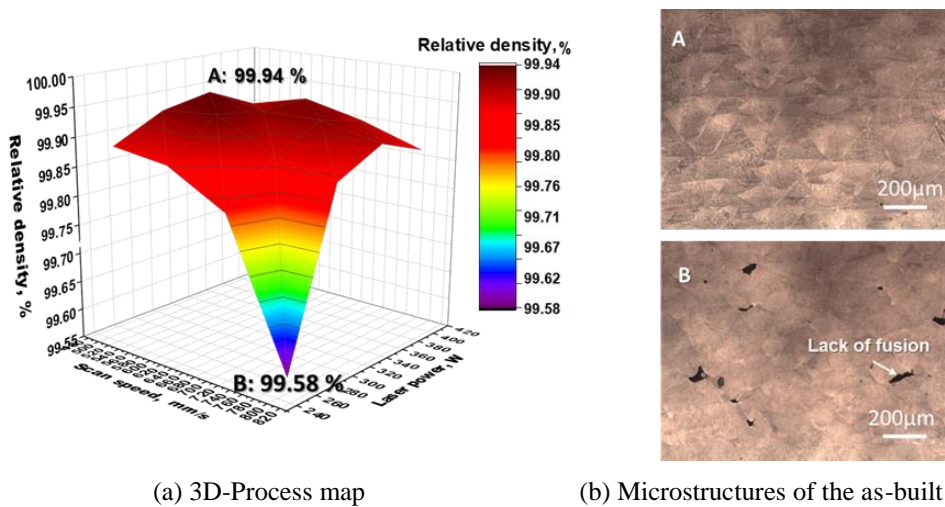
Fig.8 The 3D-Process map between laser power and scan speed evaluated by the density of cuboid specimens and the microstructures of the as-built specimens of A and B

Regarding the relation between process parameters and surface texture, Whip et al. (2019) investigated the relation between process parameters (laser power and scan speed) and seven different standard height-based surface roughness metrics. They concluded that the arithmetical mean height S_a, the maximum pit height S_v, the material ratio S_{mr2}, and the reduced dale height S_{vk} decrease with an increasing in laser power, while different trends exist with changing scan speed. Taylor et al. (2019) investigated the correlation among surface texture, energy density and density, and concluded that S_a is unsuitable for delineating between different PBF-LB parts, while the root mean square slope ($S\Delta_q$) is a better delineator. In this study, S_a and S_q were applied as the representative surface texture parameters to evaluate the surface texture of the as-built specimen. As described by Whip et al. (2019), the surface texture is greatly affected by the process parameters such as laser power and scan speed. In particular, it is considered to be difficult to evaluate the surface texture in the regions of A and C using only S_a or S_q because lots of spatters exist on the surface due to unsuitable process parameters. Whereas it is considered that S_a or S_q enables to evaluate the surface texture in the region A because a few spatters exist on the surface owing to suitable process parameters. Thus, the influence of the process parameters on the surface texture is complicated and has not been quantitatively investigated.

Consequently, it was found that the process parameters such as laser power and scan speed essentially affect not only the density but also the surface texture. Therefore, the process map is one of the effective tools to determine the optimum process parameters corresponding to the part quality characteristics such as density and surface texture. Although Hertlein et al. (2020) proposed the prediction system for AM part quality using the training data from the literatures and the hybrid Baysian network, the prediction of optimum process parameters requires the training data corresponding to the employed machine and powder in the PBF-LB process because of complicatedly tangled process

behaviors. Therefore, the real results based on the designs of experiments (DOEs) are essential to predict as accurate as possible.
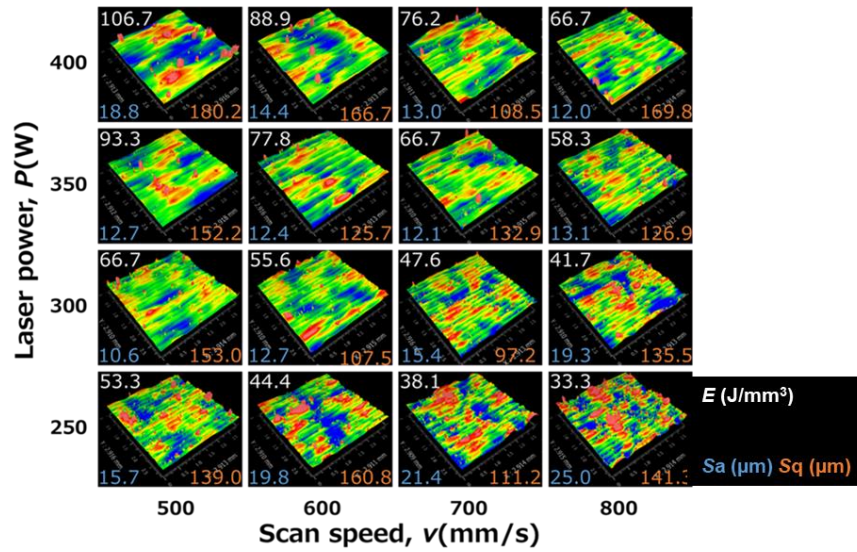

Fig. 9 The surface texture of cuboid specimens fabricated at various conditions of lower laser power and scan speed
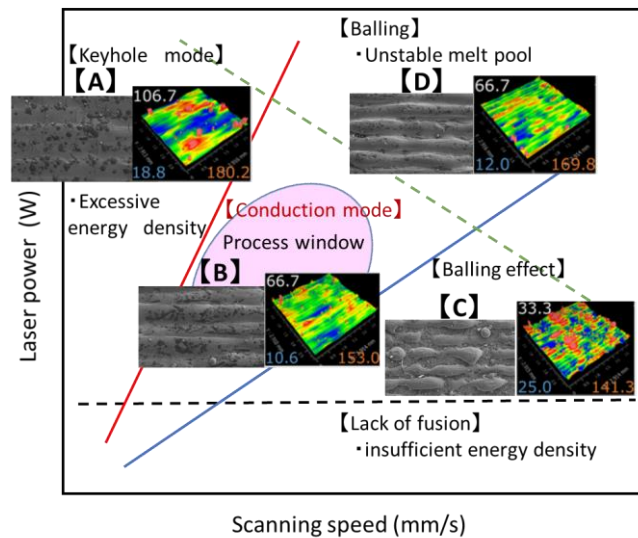

Fig. 10 The schematic process map between laser power and scan speed evaluated by surface texture

The process maps of laser power and scan speed evaluated by surface texture parameter S_a and density are depicted in Fig. 11(a) and Fig. 11(b), respectively. As shown in Fig. 11(a), the laser power and the scan speed showed the minimum surface texture are around 300 W and 500 mm/s (blue area), respectively. On the other hand, as shown Fig. 11(b), the laser power and the scan speed showed the maximum density is around 300 W and 500 mm/s (red area), respectively.

Thus, it was revealed that the optimum laser power and scan speed can be determined using the process maps evaluated by surface texture parameter and density. Moreover, the similarity of the process map of laser power and scan speed evaluated by surface texture parameter and by density suggests that there could be a correlation between surface texture and density. In our previous study (2021), the correlation between the density and 35 areal surface-texture parameters (ISO 25,178–2 standard, 2021) of manufactured specimens was investigated using the CSI equipment (Zygo NewView 9000). As a result, the correlation between the surface texture and density or internal defects was confirmed using the specific surface texture parameters. Therefore, the specific surface texture parameters may correlate with the density.
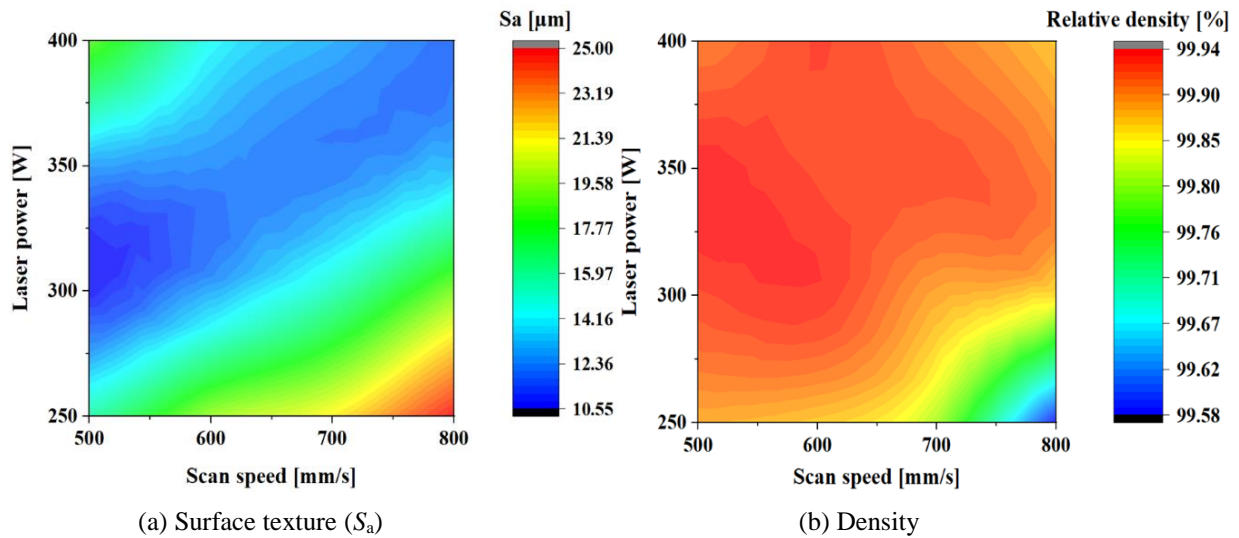
(a) Surface texture (S_a)　　　　　　　　　　(b) Density

Fig.11 The process maps between laser power and scan speed evaluated by surface texture and density of the cuboid specimens

3.3 Mechanical properties of the as-built specimens

The round bars for tensile test specimens were fabricated under the optimum fabrication condition shown in Table 4. The round bars (length: 100 mm, diameter: 14 mm) fabricated at various build directions of 0° (transverse), 45° (diagonal) and 90° (longitudinal) on the build plate are exhibited in Fig. 12.

Table 4 The fabrication conditions of tensile specimen

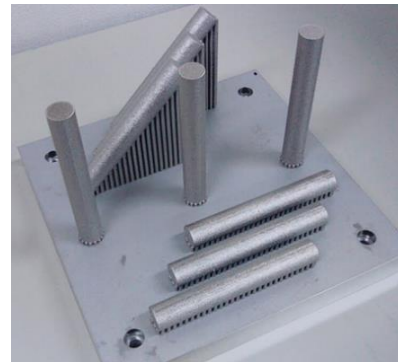|	
Laser power (W)	300
Scan speed (mm/s)	500
Hatching pitch (mm)	0.15
Layer thickness (mm)	0.05
Spot diameter (mm)	0.20
Energy density (J/mm^3)	80.0

Fig.12 The as-built round bars for tensile test specimens

The results of this work and other works of tensile tests are shown in Table 5. The as-built specimens showed anisotropic tensile behavior because of the formation of fiber texture of columnar grains, and the tensile strength of the transverse specimen was higher than that of the longitudinal specimen. Thus, the tensile properties are different in building direction. The 0.2% proof strength and tensile strength of the transverse specimen are 748 MPa and 1038 MPa, respectively, and are higher than those of the other specimens. According to the report by Chlebus et al. (2015), the tensile strength of the specimen built in the build direction (longitudinal) is considerably lower than that of the specimen built in other directions because the perpendicular orientation of overlapping interfaces between layers to the loading direction is conductive to cracking and strengthening by grain boundaries is relatively weaker. Also, Ni et al. (2017) described that the longitudinal specimen showed lower tensile strength than the transverse specimen because the {100} fiber texture of columnar grains leads to high strength in the transverse direction. The elongation of any specimen is more than 20%. Elongation of the as-built specimen is higher than that of the as-built alloy reported by Chlebus et al. (2015) and similar to that of the as-built specimen reported by Ni et al. (2017).

As a result, the tensile properties of the as-built specimen fabricated at the optimum condition determined by the evaluation of surface texture and the density are similar to those of the as-built specimen reported by the other works.

Table 5 The mechanical properties of the as-built IN 718 alloy fabricated by PBF-LB

Sample	0.2%Proof strength (MPa)	Tensile strength (MPa)	Elongation (%)	Reduction of area (%)	Ref.
Transverse	748±6.7	1038±7.7	21.9±3.2	31.5±8.5	This work
Diagonal	676±4.7	929±45.3	21.1±8.7	22.4±5.5	This work
Longitudinal	594±2.7	953±40	22.1±12.6	34.7±13.8	This work
Transverse	643±63	991±62	13±6		[Chlebus et al. (2015)]
Diagonal	590±15	954±10	20±1		[Chlebus et al. (2015)]
Longitudinal	572±44	904±22	19±4		[Chlebus et al. (2015)]
Transverse	858±12	1167±10	21.5±1.3		[Ni et al. (2017)]
Longitudinal	711±14	1110±11	24.5±1.1		[Ni et al. (2017)]
Wrought(as-rolled)	1034	1276	12		[Ni et al. (2017)]

4. Conclusions

In this study, in order to optimize the process parameters of PBF-LB for Inconel 718, the melting and solidification phenomena of the melt pool were investigated using a high-speed camera and the process map of laser power and scan speed was constructed by evaluation of surface texture and density of the as-built specimen. In addition, the mechanical properties of the as-built specimens fabricated at the optimum process parameter derived from the process map were examined. The results obtained are as follows.

(1) It is significant to determine the optimum process parameter by consideration of the melting and solidification phenomena because the phenomena such as spattering and instability of the melt pool changes with the process parameters.

(2) It was found that the morphology of the track is affected by the spot size of the laser beam, and the process window of spot size of 0.1 mm and 0.2 mm is wider than that of 0.3 mm.

(3) The surface texture was strongly affected by the melting and solidification behavior of the melt pool. It was found from the process map that the suitable energy density is around 80 J/mm^3 to fabricate the specimens having a smooth surface. In the case of laser power of 300 W and a scan speed of 500 mm/s, that is, an energy density of 80 J/mm^3, the minimum S_a was 10 µm.

(4) The relative density increased with increasing the energy density and the maximum relative density was 99.94% at a laser power of 300 W and a scan speed of 500 mm/s (an energy density of 80 J/mm^3).

(5) It was revealed that the optimum laser power and scan speed using the process maps evaluated by surface texture was similar to that evaluated by density. This result suggests that the surface texture of the specimen could correlate with the density.

(6) The tensile properties of the as-built specimen fabricated at the optimum condition determined by the evaluation of surface texture and the density was similar to those of the as-built specimen reported by the other works.

Acknowledgments

References

Amato, K.N., Gaytan, S.M., Murr, L.E., Martines, E., Shindo, P.W., Hernandes, J., Collins, S. and Medina, F., Microstructures and mechanical behavior of Inconel 718 fabricated by selective laser melting, Acta Materialia, Vol.60, No.5 (2012), pp.2229-2239.

Aoyagi, K., Wang, H., Sudo, H. and Chiba, A., Simple method to construct process maps for additive manufacturing using a support vector machine, Additive Manufacturing, Vol.27, (2019), pp.353–362.

ASM International Handbook Committee, Metals Handbook Desk Edition, 2nd ed. (1998), pp.394-414, ASM.

Aydinoez, M.E., Brenne, F., Schper, M., Schaak, C., Tillmann, W., Nellesen, J. and Nienodorf, T., On the microstructural and mechanical properties of post-treated additively manufactures Inconel 718 superalloy under quasi-static and cyclic loading, Materials Science and Engineering A, Vol.669, (2016), pp.246-258.

Baturynska, I., Semeniuta, O. and Martinsen, K., Optimization of process parameters for powder bed fusion additive manufacturing by combination of machine learning and finite element, Procedia CIRP, Vol.67, (2018), pp.227-232.

Bean, G.E., Witkin, D.B., McLouth, T.D., Patel, D.N. and Zaldivar, R., Effect of laser focus shift on surface quality and density of Inconel 718 parts produced via selective lase melting, Additive Manufacturing, Vol.22, (2018), pp.207-215.

Caggiano, A., Zhang, J., Alfieri, V., Caiazzo, F., Gao, R., Teti, R., Machine learning-based image processing for on-line defect recognition in additive manufacturing, CIRP Annals - Manufacturing Technology, Vol.68, No.1 (2019), pp. 451-454.

Carter, L.N., Essa, K. and Attallah, M.M., Optimisation of selective laser melting for a high temperature Ni-superalloy, Rapid Prototyping J., Vol.21, No.4 (2015), pp.423-432.

Chlebus, E., Gruber, K., Kuznicka, B., Kurzac, J. and Kurzynowski, T., Effect of heat treatment on the microstructure and mechanical properties of Inconel 718 processed by selective laser melting, Materials Science and Engineering A, Vol.639, (2015), pp.647-655.

Cunningham, R., Zhao, C., Parab, N., Kantzos, C., Pauza, J., Fezzaa, K., Sun, T. and Rollett, A.D., Keyhole threshold and morphology in laser melting revealed by ultrahigh-speed x-ray imaging, Science, Vol.363, No.6429 (2019), pp.849-852.

Ferber, B., Small, K.A., Allen, C., Gauston, R.J., Nicohls, A., Simbolick, J. and Taheri, M.L., Correlation of mechanical properties to microstructure in Metal Laser Sintering Inconel 718, Materials Science and Engineering A, Vol.712, (2018), pp.539-547.

Fleming, T.G., Nestor, S.G.L., Allen, T.R., Boukhaled, M.A., Smith, N.J. and Fraser, J.M., Tracking and controlling the morphology evolution of 3D powder-bed fusion in situ using inline coherent imaging, Additive Manufacturing, Vol.32, (2020), 100978.

Forien, J.-B., Calta, N.P., DePond, P.J., Guss, G.M., Roehling, T.T. and Matthews, M.J., Detecting keyhole pore defects and monitoring processsig natures during laser powder bed fusion: A correlation between insitu pyrometry and exsitu X-ray radiography, Additive Manufacturing, Vol.35, (2020), 101336.

Fu, S.H., Dong, J.X., Zhang, M.C. and Xie, X.S., Alloy design and development of INCONEL718 type alloy, Materials Science and Engineering A, Vol.499, (2009), pp.215-220.

Furumoto, T., Egashira, K., Munekage, K., Abe, S., Experimental Investigation of Melt Pool Behaviour During Selective Laser Melting by High Speed Imaging, CIRP Annals Manufacturing Technology, Vol.67, No.2 (2018), pp.253-256.

Gibson, I., Rosen, D.W. and Stucker, B., Additive Manufacturing Technologies (2010), Springer.

Gobert, C., Reutzel, E. W., Petrich, J., Nassar, A.R. and Phoha, S., Application of supervised machine learning for defect detection during metallic powder bed fusion additive manufacturing using high resolution imaging, Additive Manufacturing, Vol.21, (2018), pp.517–528.

Grasso, M., Colosimo, B.M., Process Defects and in situ Monitoring Methods in Metal Powder Bed Fusion: a Review. Measurement Science & Technology, Vol.28, No.4 (2017), 28044005.

Hertlein, N., Deshpande, S., Venugopal, V., Kumar, M. and Anand, S., Prediction of selective laser melting part quality using hybrid Bayesian network, Additive Manufacturing, Vol.32, (2020), 101089.

Ikeshoji, T.-T., Nakamura, K., Yonehara, M., Imai, K. and Kyogoku, H., Selective laser melting of pure copper, JOM, Vol.70, (2018), pp.396-400.

ISO25178-2: Geometrical product specifications [GPS] – Surface texture: Areal – Part 2 (2021).

Jia, Q. and Gu, D., Selective laser melting additive manufacturing of Inconel 718 superalloy parts: Densification, microstructure and properties, J. Alloys and Compounds, Vol.585, (2014), pp.713-721.

Khairallah, S.A., Anderson, T., Rubenchik, A.M. and King, W.E., Laser powder-bed fusion additive manufacturing: Physics of complex melt flow and formation mechanisms of pores, spatter, and denudation zones, Acta Materialia, Vol.108, (2016), pp.36-45.

Khairallah, S.A., Martin, A.A., Lee, J.R.I., Guss, G., Calta, N.P., Hammons, J.A., Nielsen, M.H., Chaput, K., Schwalbach, E., Shah, M.N., Chapman, M.G., Willey, T.M., Rubenchik, A.M., Anderson, A.T., Wang, Y. M., Matthews, M.J. E. and King, W.E., Controlling interdependent meso-nanosecond dynamics and defect generation in metal 3D printing, Science, Vol.368, No.6491 (2020), pp.660–665.

King, W.E., Barth, H.D., Castillo, V.M., Gallegos, G.F., Gibbs, J.W., Hahn, D.E., Kamath, C. and Rubenchik, A.M., Observation of keyhole-mode laser melting in laser powder-bed fusion additive manufacturing, J. Materials Processing Technology, Vol.214, No. 12 (2014), pp.2915-2925.

King, W.E., Anderson, T., Ferencz, R.M., Hodge, N.E., Kamath, C. and Khairallah, S.A., Overview of modelling and simulation of metal powder bed fusion process at Lawrence Livermore National Laboratory, Materials Science and Technology, Vol.31, No. 8 (2015), pp.957-968.

Kirka, M.M., Medina, F., Dehoff, R. and Okello, A., Mechanical behavior of post-processed Inconel 718 manufactured through the electron beam melting process, Materials Science and Engineering A, Vol.680, (2017), pp.338-346.

Kyogoku, H. and Ikeshoji, T.-T., A review of metal additive manufacturing technologies: Mechanism of defects formation and simulation of melting and solidification phenomena in laser powder bed fusion process, Mechanical Engineering Reviews, Vol.7, No.1 (2020), DOI: 10.1299/mer.19-00182.

Ly, S., Rubenchik, A.M., Khairallah, S.A., Guss, G. and Matthews, M.J., Metal vapor micro-jet controls material redistribution in laser powder bed fusion additive manufacturing, Scientific Reports, Vol.7, (2017), 4085.

Martin, A.A., Calta, N.P., Khairallah, S.A., Wang, J., Depond, P.J., Fong, A.Y., Thampy, V., Guss, G.M., Kiss, A.M., Stone, K.H., Tassone, C.J., Weker, J.N., Toney, M.F., van Buurenl, T. and Matthews, M.J., Dynamics of pore formation during laser powder bed fusion additive manufacturing, Nature Communications, Vol.10, (2019), 1987.

Matthews, M.J., Guss, G., Khairallah, S.A., Rubenchik, A.M., Depond, P.J. and King, W.E., Denudation of metal powder layers in laser powder bed fusion processes, Acta Materialia, Vol.114, (2016), pp.33-42.

McLouth, T.D., Bean, G.E., Witkin, D.B., Sitzman, S.D., Adams, P.M., Patel, D.N., Park, W., Yang, J.-M. and Zaldivar, R., The effect of laser focus shift on microstructural variation of Inconel 718 produced by selective laser melting, Materials and Design, Vol.149, (2018), pp.205-213.

Nadammal, N., Cabeza, S., Mishurova, T., Thiede, T., Kromm, A., Seyfert, C., Farahbod, L., Haberland, C., Schneider, J.A., Portella, P.D. and Bruno, G., Effect of hatch length on the development of microstructure, texture and residual stresses in selective laser melted superalloy Inconel 718, Materials and Design, Vol.134, (2017), pp.139-150.

Ni, M., Chen, C., Wang, X., Wang, P., Li, R., Zhang, X. and Zhou, K., Anisotropic tensile behavior of in situ precipitation strengthened Inconel 718 fabricated by additive manufacturing, Materials Science and Engineering A, Vol.701, (2017), pp.344–351.

Sames, W.J., Unocic, K.A., Helmreich, G.W., Kirka, M.M., Medina, F. and Dehoff, R.R., Feasibility of in situ controlled heat treatment (ISHT) of Inconel 718 during electron beam melting additive manufacturing, Additive Manufacturing, Vol.13, (2017), pp.156-165.

Taylor, S., Jared, B., Koepke, J., Forrest, E. and Beaman, J., Investigating Applicability of Surface Roughness Parameters in Describing the Metallic AM Process, Sandia National Lab. (SNL-NM) (Albuquerque, NM, United States) (2019).

Whip, B., Sheridan, L. and Gockel, J., The effect of primary processing parameters on surface roughness in laser powder bed additive manufacturing, Int. J. Advanced Manufacturing Technology, Vol.103, (2019), pp.4411–4422.

Yakout, M., Cadamuro, A., Elbestawi, M. A. and Veldhuis, S. C., The selection of process parameters in additive manufacturing for aerospace alloys, Int. J. Advanced Manufacturing Technology, Vol.92, (2017), pp.2081–2098.

Yonehara, M., Kato, C., Ikeshoji, T.-T., Takeshita, K. and Kyogoku, H., Correlation between surface texture and internal defects in laser powder-bed fusion additive manufacturing, Scientific Reports, Vol.11, (2021), 22874.

Zhang, D., Niu, W., Cao, X. and Liu, Z., Effect of standard heat treatment on the microstructure and mechanical properties of selective laser melting manufactured Inconel 718 superalloy, Materials Science and Engineering A, Vol.644, (2015), pp.32-40.

Zhao, C., Fezzaa, K., Cunningham, R.W., Wen, H., De Carlo, F., Chen, L., Rollett, A.D. and Sun, T., Real-time monitoring of laser powder bed fusion process using high-speed X-ray imaging and diffraction, Scientific Reports, Vol.7, (2017), 3602.